Physica Medica 63 (2019) 87–97

Contents lists available at ScienceDirect

Physica Medica

journal homepage: www.elsevier.com/locate/ejmp

Original paper

Design optimization of a pixel-based range telescope for proton computed tomography

Helge Egil Seime Pettersen[a,*], Johan Alme[b], Gergely Gábor Barnaföldi[c], Rene Barthel[d], Anthony van den Brink[d], Mamdouh Chaar[b], Viljar Eikeland[b], Alba García-Santos[d], Georgi Genov[b], Silje Grimstad[e], Ola Grøttvik[b], Håvard Helstrup[e], Kristin Fanebust Hetland[e], Shruti Mehendale[b], Ilker Meric[f], Odd Harald Odland[a,b], Gábor Papp[g], Thomas Peitzmann[d], Pierluigi Piersimoni[b], Attiq Ur Rehman[b], Matthias Richter[h], Andreas Tefre Samnøy[b], Joao Seco[i,j], Hesam Shafiee[b,f], Eivind Vågslid Skjæveland[f], Jarle Rambo Sølie[b,f], Ganesh Tambave[b], Kjetil Ullaland[b], Monika Varga-Kofarago[c], Lennart Volz[i,j], Boris Wagner[b], Shiming Yang[b], Dieter Röhrich[b]

[a] Department of Oncology and Medical Physics, Haukeland University Hospital, 5021 Bergen, Norway
[b] Department of Physics and Technology, University of Bergen, 5020 Bergen, Norway
[c] Department for Theoretical Physics, Heavy-Ion Research Group, Wigner RCP of the Hungarian Academy of Sciences, 1121 Budapest, Hungary
[d] Institute for Subatomic Physics, Utrecht University/Nikhef, Utrecht, Netherlands
[e] Department of Computing, Mathematics and Physics, Western Norway University of Applied Science, 5020 Bergen, Norway
[f] Department of Electrical Engineering, Western Norway University of Applied Sciences, 5020 Bergen, Norway
[g] Institute for Physics, Eötvös Loránd University, 1/A Pázmány P. Sétány, H-1117 Budapest, Hungary
[h] Department of Physics, University of Oslo, 0371 Oslo, Norway
[i] Department of Biomedical Physics in Radiation Oncology, German Cancer Research Center, Heidelberg, Germany
[j] Department of Physics and Astronomy, Heidelberg University, Heidelberg, Germany

ARTICLE INFO

Keywords:
Proton computed tomography
Detector optimization
Monte Carlo simulation
Track reconstruction

ABSTRACT

Purpose: A pixel-based range telescope for tracking particles during proton imaging is described. The detector applies a 3D matrix of stacked Monolithic Active Pixel Sensors with fast readout speeds. This study evaluates different design alternatives of the range telescope on basis of the protons' range accuracy and the track reconstruction efficiency.

Method: Detector designs with different thicknesses of the energy-absorbing plates between each sensor layer are simulated using the GATE/Geant4 Monte Carlo software. Proton tracks traversing the detector layers are individually reconstructed, and a Bragg curve fitting procedure is applied for the calculation of each proton's range.

Results: Simulations show that the setups with 4 mm and thinner absorber layers of aluminum have a low range uncertainty compared to the physical range straggling, systematic errors below 0.3 mm water equivalent thickness and a track reconstruction capability exceeding ten million protons per second.

Conclusions: In order to restrict the total number of layers and to yield the required tracking and range resolution properties, a design recommendation is reached where the proposed range telescope applies 3.5 mm thick aluminum absorber slabs between each sensor layer.

1. Introduction

Proton Computed Tomography (proton CT) is an imaging modality able to measure the proton stopping power of the patient prior to treatment planning and treatment in proton therapy [1]. The goal of proton CT is to increase the accuracy of the proton range estimation, compared to conversion from the X-ray mass attenuation using X-ray CT [2]. Several design approaches for proton CT have been proposed. Usually, tracker planes in front of and behind the patient measure each proton's position and direction so that their path through the patient

* Corresponding author.
E-mail address: helge.pettersen@helse-bergen.no (H.E.S. Pettersen).

https://doi.org/10.1016/j.ejmp.2019.05.026
Received 31 December 2018; Received in revised form 23 April 2019; Accepted 28 May 2019
Available online 06 June 2019

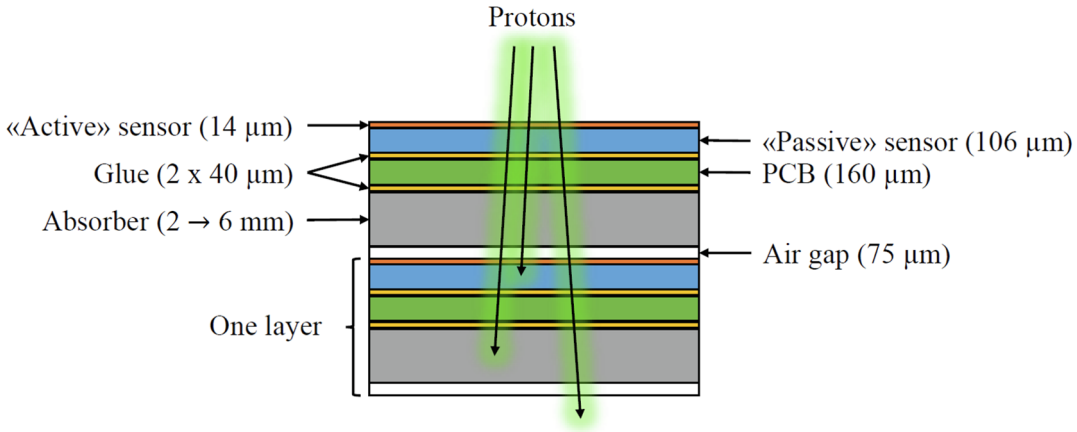

Fig. 1. The design to be optimized: Different thicknesses (2–6 mm) for the energy absorbers are evaluated through MC simulations. To fully slow down and stop a 230 MeV proton beam, 25–65 layers are needed depending on the thickness of the absorbers. Only the "active" sensor volumes are used as sensitive volumes in the MC simulations [7].

can be estimated [3,4]. The residual range (or energy) of each proton is then measured using range telescopes or scintillator calorimeters. Position-sensitive range telescopes have been proposed in Esposito et al. [5] with silicon strip detectors and in Pettersen et al. [6] with pixel detectors: these systems are able to measure a high number of protons in a single readout cycle, thereby increasing the proton intensity capacity.

The aim for this study is to optimize the various properties of the design of a pixel-based range telescope for proton CT. The simultaneous optimization of the following metrics is performed: accuracy and precision of the range determination; high track reconstruction efficiency, *i.e.* the ability to disentangle and reconstruct all incident protons in a single readout frame; and other constraints such as cost (the number of layers), cooling and mechanical stability. We apply the experience from a proof-of-concept detector [6] in order to propose a design for a next prototype currently under development [7].

The range accuracy will have impact on the degree to which the proton stopping power of the patient can be correctly calculated. A low range uncertainty and an efficient track reconstruction enable lower required proton intensities during the scan, *i.e.* a lower dose to the patient, shorter scan times and a higher SNR.

The design optimization of this study is performed through the determination of an optimized thickness of the energy absorber material between the sensor layers, as well as the choice of the absorber material. Several different values for the thicknesses are evaluated by means of Monte Carlo (MC) simulations, using the GATE 8.1.p01 [8–10]/Geant4 10.4.p02 software [11,12].

1.1. The ALPIDE pixel chip

The sensor chip for the range telescope is the ALice PIxel DEtector (ALPIDE) chip [13], which is a Monolithic Active Pixel Sensor (MAPS) with a 1-bit digital "hit-or-no-hit" readout based on a pre-set threshold. The planned upgrade of the ALICE Inner Tracking System (ITS) at CERN-LHC is based on the ALPIDE chip, which has been developed for that specific purpose [14]. Each chip has an active area of approximately $3 \times 1.5\,cm^2$: from a 1024×512 pixel array of $29.24 \times 26.88\,\mu m^2$ pixels. The chip has a fast programmable integration time of ~5–10 μs (corresponding to 100,000 frames per second) and is capable of handling a continuous readout at that rate. The readout rate is achieved by data reduction through regional pixel readout via a priority encoder, a multi-event memory and a *zero-suppression* technique where only activated pixels send a signal. More details on the integration of the ALPIDE chips into the proton CT system can be found in Grøttvik [15].

Since the ALPIDE chips have a 1-bit digital readout per pixel, it is not possible to directly measure the energy deposited in each pixel. This is in contrast to *e. g.* the Timepix pixel sensor [16], where the deposited energy of traversing charged particles can be accurately calculated [17]. However, Maczewski [18] and Pettersen [7] propose models for determining the energy deposited by means of counting the number of activated pixels in the area surrounding a proton track. These models, when adapted to the ALPIDE chips, are expected to aid in the reconstruction of proton tracks and the filtering of secondary particles (if the energy deposition signatures of the particles are sufficiently separated for discrimination by cluster size). A method of generating realistic pixel clusters in the MC simulations is described in Section 3.4.

2. Detector design guidelines

The proton CT system is to consist of 25–65 layers stacked longitudinally (the number of layers is determined by their design). Each layer is an assembly of small-area ALPIDEs yielding a large sensitive area, which is glued to a flexible PCB cable, again glued to an energy-absorbing slab of a suitable material. It is possible to define a large number of potential designs for the detector, and therefore some constraints must be put on the degrees of freedom in this work. A baseline design based on the original prototype from Nooren et al. [19], and adapted to proton CT in Pettersen et al. [6], is shown in Fig. 1. The geometry of the sensor chips and the electronic components are kept from the original design, while the energy absorbers between the sensor layers are varied in the range between 2 mm and 6 mm aluminum (this material choice is discussed in the following).

In order to achieve a high accuracy in the measurement of the initial proton vectors, the two first sensor-absorber layers in the range telescope should contain as little mass as possible [20]. To this end, the first absorber layer is replaced with a low-mass stabilizer.

The purpose of this study is to determine the optimal absorber thickness in terms of range accuracy and proton track reconstruction. This result determines the total number of detector layers needed in the final prototype. Details such as chip bonding, aspects related to the mechanical structure, heat sink design and the readout electronics are out of scope of this work and, also, not yet finally decided upon. As a result of this, the exact results of the simulations will not reflect the detailed final prototype. Several simplifications are made during in the design configurations for the MC simulations, such as using homogeneous slabs of materials rather than implementing accurate designs with details such as the ALPIDE chips bonded to the PCB, glued to a backing together with absorbers and heat sinks, all mounted to a scaffolding. Nevertheless, the longitudinal distribution of materials will

Table 1
Properties of the potential absorber materials [24–26,7,27]. The scattering angle is calculated using Eq. (1).

Material	PMMA	Carbon Fiber	Aluminum	Copper	Tungsten
4 mm WET [mm]	3.46	2.24	1.9	0.66	0.4
4 mm WET scattering angle [mrad]	9.0	10.9	14.6	21.4	33.8
4 mm WET neutron yield [10− 4]	69.2	71.9	80.9	74.1	26.9
Thermal conductivity [W/mK]	0.25	800	205	401	174
Thermal expansion [$10^{-6}K^{-1}$]	70	2–4	21–24	16	4.5

be modeled and included to the level of available knowledge.

2.1. The absorber material

Properties such as proton stopping- and scattering power, durability, ease of machining and mounting, thermal conductivity, thermal expansion of the absorber material and secondary neutron production must be considered for the absorber material, as well as the interface between the absorber and the aluminum carrier board for the sensor chips (*e.g.* having similar thermal expansion coefficients). See Table 1 for a list of different properties: the water equivalent thickness (WET) is found by finding the thickness which yields the same energy loss as 4 mm water. The angular dispersion in a thin layer due to MCS can be calculated using the Rossi-Greisen equation [21]:

$$\sigma_{\mathrm{MCS}} = \frac{21.1}{\sqrt{2}} \frac{1}{\beta p} \sqrt{\frac{x}{X_0}} \simeq 0.1 \sqrt{\frac{x}{X_0}}, \tag{1}$$

where βp are the kinematic variables for momentum and velocity, X_0 is the radiation length and x is the layer thickness. The last approximation in the equation holds for the energies of interest [22]. The scattering angle is calculated for a therapeutic proton through a 4 mm WET slab.

The neutron yield is the number of neutrons produced per incoming proton (150 MeV beam in a slab of 4 mm WET, found in the GATE simulations by using the `QGSP_BIC_HP` physics builder list and 10^5 primaries. The Poisson error from this procedure is 4%–6%).

Based on these, and in particular that the flexible PCB cables connected to the ALPIDE sensors are mounted to an aluminum backing, and when considering the ease of machining, the material of choice for the absorber is aluminum.

In terms of the stabilization of the first low-mass tracker layers, carbon fiber is a natural choice due to its thermal properties, low mass and structural stability. Carbon fiber stabilization is also being explored in the context of the ALPIDE sensors in the ALICE-ITS upgrade [14,23]. The effect of scattering in the first low-mass layers on the proton trajectory estimation error is theoretically demonstrated in Section 6.4.

3. Monte Carlo simulations

3.1. Geometry setup

To perform the data analysis in order to calculate the desired performance metrics, the MC simulations must contain the following: a proton beam with realistic spatial and (adjustable) spectral characteristics, and a sufficiently accurate geometrical implementation of a stack of the ALPIDE chips and the absorber layers of adjustable thicknesses.

A water phantom of variable thickness is used to slow down a 250 MeV proton beam, in order to represent realistic energy spectra with residual proton ranges that span the complete detector in depth. The water phantom thicknesses vary from zero to the maximum water equivalent range of the beam, approximately 38 cm, in steps of 1 mm, as shown in Fig. 2. A pencil beam is here modeled as a Gaussian with standard deviation 3 mm, placed 10 cm in front of the energy degrading water phantom. Its divergence is 2 mrad, and the emittance is 15 mm mrad [28]. The environment around the setup is modeled as air.

3.2. Simulation parameters

The simulations have been performed using GATE 8.1.p01 [8–10] together with Geant4 10.4.p02 [11,12]. The physics builder list `QGSP_BIC_EMZ` is used, adjusted with a mean ionization potential for water of 75 eV for agreement with the PSTAR database [29], which is used to calculate and compare the energy loss of protons through the energy modulating water phantom. This builder list includes the Geant4 Bertini intranuclear Cascade model for production of secondary protons and neutrons through inelastic nuclear collisions, and the “option 4” electromagnetic physics list designed for simulations requiring high accuracy, as recommended by Grevillot et al. [30]. The default value for the secondary production threshold of 0.7 mm is kept. The global step size is set at 0.5 mm together with the parameter dOverRange = 0.2, which limits the step size relative to the remaining range [12].

A sensitivity analysis of the applied physics models has been carried out, this to validate that the pertinent metrics such as proton range, relevant secondary particle production (and detection) and energy deposition in the epitaxial layers do not change when the particle step size and production thresholds are reduced by an order of magnitude (using a global step size of 50 μm, and a production range threshold of 50 μm). The charge diffusion of low-energy electrons inside the epitaxial layer of the ALPIDE sensor is not simulated, and is instead modeled using experimental data as described in Section 3.4.

The simulations have been carried out using 100,000 primary protons for each water phantom thickness, for each of the aluminum absorber thickness designs. This number represents a balance between the total CPU requirements (5 geometries × 360 energies × 10^5 primaries) and the statistical quality of the distributions to be fitted (see Fig. 4). The simulations require approximately 320 total CPU-hours on an Intel ® Xeon ® Gold 6136 (3.0 GHz). Additionally, the track reconstruction process (excluding the pixel clustering model) requires approximately 1.2 ms per track per CPU on the same system.

3.3. Proton range from “MC truth”

In the “MC truth” simulations, the complete detector geometry (including the aluminum absorbers) is setup as sensitive volumes to achieve a high accuracy of the residual proton ranges. In this case, for computational requirements, the number of primaries is reduced to 15,000 per water phantom degrader thickness and per absorber thickness. A look-up-table (LUT) containing phantom thicknesses, proton energies incident on the detector and residual ranges is created, to be retrieved using a cubic spline interpolation. The LUT was used during analysis to evaluate the accuracy of the range calculations. This LUT-based approach has been shown to yield a high proton range accuracy [31].

3.4. Pixel clustering model

The monolithic design of the ALPIDE sensors allows charge carriers in the epitaxial layer to diffuse freely between the pixels. Thus, a traversing proton with a relatively high energy loss will create a charge cloud that activates 1–30 pixels around the track. This process involves electrons of thermal energies and is not directly simulated in this study. If a reverse-substrate bias voltage is applied across the epitaxial layer,

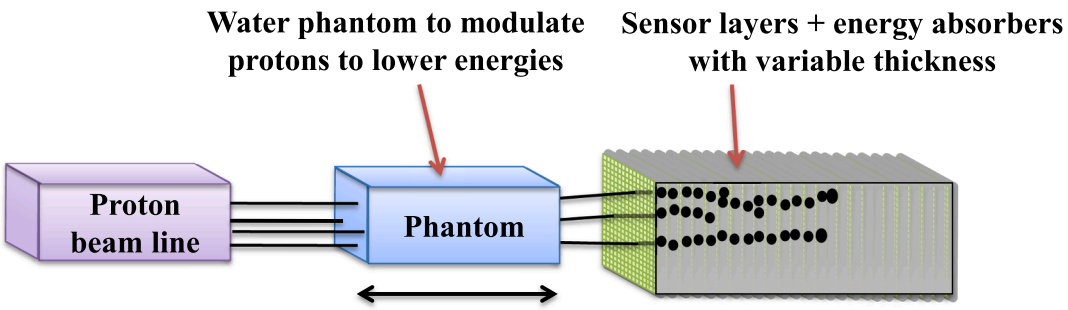

Fig. 2. Schematic setup of the range calculation geometry. In order to obtain proton beams of different energy spectra from a 250 MeV beam, the thickness of the energy degrading water phantom is modulated from 0 cm to the maximum range of a 250 MeV beam, which corresponds to a water phantom length of approximately 38 cm [7].

the charge carriers are collected quicker and the number of activated pixels is reduced significantly [32].

In a recent experimental beam test at the Heidelberg Ion Therapy facility[1], a three-layer telescope made up of three single ALPIDE chips was irradiated by protons of energies 48.12 MeV, 200.11 MeV and 221.06 MeV, and helium ions of energies 50.57 MeV/u, 150.11 MeV/u, 100.19 MeV/u, 200.38 MeV/u and 220.5 MeV/u (results to be published).

Subsequent analysis using the PSTAR database [29] yielded a correlation between the calculated deposited energy inside the epitaxial layers, E_D [keV/μm], and the (average) number of activated pixels, n, around the proton track. Here, a power fit to the data is used as $n = 4.23 \cdot E_D^{0.65}$.

A library containing the observed cluster shapes and their occurrence probability was created from the same experimental data. In the following, the MC data is convoluted with the following clustering model: First, the $E_{D,i}$ from MC is used to determine the cluster size n_i using the power fit. Then, a random cluster of cluster size n_i is retrieved from the library and it is painted around the MC hit position.

The de-clustering of the resulting data is done as described in Pettersen et al. [6], where directly connected activated pixels (along the pixel sides and not diagonally) are assumed to belong to the same track crossing the sensor layer.

Unless explicitly specified otherwise, the pixel clustering model has been applied during the MC simulations in all results shown below.

4. Track reconstruction

One of the strengths of the high-granularity pixel-based detector design is the ability to disentangle and reconstruct a large number of concurrent proton tracks. To this end, a track reconstruction method has been developed, with more details in Pettersen et al. [33]. As an improvement to that algorithm, here we start the reconstruction process by choosing seeds from the distal end of the detector, such that the depths of both the starting and stopping position of each proton are known prior to reconstruction: this is, respectively, the first sensor layer and the distal sensor layer where the seed is located. The reconstruction is first started from the last layer containing data, then the seed layer is moved sequentially towards the first sensor layer until all identifiable tracks have been accounted for.

A seed is chosen from the last traversed detector layer. Track candidates are grown towards the detector front face, each track segment chosen to minimize the distance between the extrapolated position and actual position of the candidate hit in the next layer. A track weight $S_n = \sqrt{\sum_{\text{layer}}^{n} (\Delta\theta_{\text{layer}})^2}$ is calculated, based on the accumulated angular change throughout the track, up to layer n. If $S_n > S_{\max}$ the track (segment) is discarded. If several track segment candidates are available, the best two are kept if they are sufficiently similar (both are kept if the next-to-best candidate's S_n value is at most 15% higher, otherwise, only the best is kept). This procedure has been implemented in order to avoid an exponentially growing number of track candidate splittings (one per layer). To account for close hits with merged clusters, the algorithm skips a layer if no clusters have been found at the extrapolated track's position.

The choice of $S_{\max}$ is based on the expected scattering in the detector, and on the track density: higher track densities require a smaller $S_{\max}$ in order to avoid confusion. The procedure to find the optimal $S_{\max}$ value is based on a parameter scan of different $S_{\max}$ values applied on the track reconstruction of pencil beams—in Pettersen et al. [33] values of 150–300 mrad are identified, depending on the particle density.

4.1. Secondary tracks

The protons have a certain probability of undergoing elastic and inelastic nuclear interactions throughout both the imaged object and inside the detector itself. Secondary tracks and tracks that eventually undergo inelastic nuclear interactions potentially degrade the range accuracy. These tracks are tagged in the MC simulations, and are here collectively called secondaries.

After the reconstruction process, filters on the resulting tracks are applied. To remove tracks from non-multiple Coulomb scattering processes in the phantom, 3σ filters on the incoming angles and residual ranges are used [1]. In addition, a filter is put on the deposited energy ($E_D > 2.5$ keV/μm) in the last traversed layer in order to remove tracks undergoing inelastic collisions in the detector, and tracks that are otherwise incompletely reconstructed [7].

4.2. The correctly reconstructed track

In order to benchmark the precision and efficiency of the track reconstruction algorithm, a definition of a correctly reconstructed track must be made: The first and last entry in a track must originate from the same proton history (identified by the `eventID` tag in GATE); and the last traversed (stopping) layer must be included in the reconstructed track. By following this definition, these tracks have the correct incoming vector and the correct residual range, which are the required values for volumetric reconstruction of the stopping power map for proton CT purposes.

The *efficiency* of the track reconstruction is defined to be the ratio of correctly reconstructed tracks to the total number of tracks surviving the applied data filters.

5. Range calculation

After the track reconstruction process, each track contains a number of cluster objects: ideally one cluster for each sensor layer in the proton's trajectory. The cluster objects contain their position and cluster

[1] Conducted in July 2018.

size/deposited energy.

A Bragg curve fitting methodology is applied to find the reconstructed range $\hat{R}$ of a reconstructed proton track [6]. The mean range $\langle\hat{R}\rangle$ and the corresponding mean range uncertainty $\langle\hat{\sigma}_R\rangle$ are found for each beam energy using Eq. (3). Any fluctuations of the range accuracy relative to the proton range are also identified.

5.1. Range calculation

The pristine Bragg curve, describing a single proton's depth-dependent energy loss, can be characterized using its depth z and true range R, together with the differentiated Bragg-Kleeman equation of Bortfeld [34]:

$$-\frac{dE}{dz} = \frac{p\alpha^{1/p}}{(R-z)^{1/p-1}}, \tag{2}$$

where p and α are model parameters fitted to the "MC truth" range-energy data. For the 4 mm aluminum absorber geometry, the parameters are $\alpha = 0.0211$, $p = 1.639$. This energy-range model was shown to yield a high accuracy in Pettersen et al. [31].

Least-squares fits of the reconstructed track's energy loss in each sensor layer to Eq. (2) is performed to obtain $\hat{R}$. The energy loss used is the one calculated from the cluster sizes. Examples of the model fits overlaid on the reconstructed tracks from different geometries are shown in Fig. 3. Note that the $\hat{R}$ values found using thinner absorber designs yields a higher range determination accuracy of individual proton tracks ($\hat{\sigma}_R$).

The "MC truth" range distribution of protons at the same initial energy is approximately Gaussian. However, the range distribution originating from the Bragg curve fitting is not Gaussian, and it is not trivial to describe the variations analytically due to the nature of the sparse measurements from each sensor layer: see Fig. 4. However, a simple histogram calculation of the empirical mean value and standard deviation yields accurate results for the residual range $\langle\hat{R}\rangle$ and range uncertainty $\langle\hat{\sigma}_R\rangle$, respectively. The ranges of all protons in a beam (or in a voxel bin when performing the image reconstruction) contribute to a histogram with bin values z_i and bin heights w_i. The lower and upper limits for the range distribution z_1 and z_2, respectively, are defined as the $\mu \pm 4\sigma$ values of an initial Gaussian fit. Then, we have

$$\langle\hat{R}\rangle = \frac{\sum_{i=z_1}^{z_2} w_i z_i}{\sum_{i=z_1}^{z_2} w_i}, \qquad \langle\hat{\sigma}_R\rangle = \sqrt{\frac{\sum_{i=z_1}^{z_2} w_i (z_i - \langle\hat{R}\rangle)^2}{\left[\sum_{i=z_1}^{z_2} w_i\right] - 1}} \tag{3}$$

The above procedure is similar to the analysis of the proof-of-concept prototype [6], with the difference being the method of initially fitting the Gaussian distributions to the histogram values. In the geometries described here, a higher number of sensor layers are contained within a range distribution relative to the proof-of-concept prototype, and a higher accuracy of $\langle\hat{R}\rangle$ is expected.

5.2. Range accuracy and range uncertainty

The range accuracy and range uncertainty resulting from a specific absorber design can be found by comparing the mean "MC truth" proton range R to the mean of the reconstructed proton range distribution $\langle\hat{R}\rangle$. The range accuracy, $\langle\langle\hat{R}\rangle - R\rangle$, is found by comparing the systematic error of the mean value of the range distribution throughout the full dynamic range of the detector (in terms of proton range). The range uncertainty is found by comparing the widths of the two distributions, respectively, σ_R and $\langle\hat{\sigma}_R\rangle$. Any additional width of the reconstructed range distribution is due to the degrading effects of the sparse sampling and to the analysis routine.

Since the range uncertainty due to range straggling is known from theory [34] and from the MC simulations, the intrinsic range uncertainty from the analysis can be calculated by subtracting in quadrature the expected range straggling from the measured range uncertainty.

It is not expected that the uncertainty and accuracy for a given geometry are the same at different incident proton energies, as the values are dependent on the relative position between the proton range position versus the sensor layer position: This effect was clearly seen in Pettersen et al. [6] where the absorbers consisted of 4.3 mm tungsten (having the same water equivalent thickness as 20.4 mm aluminum at 150 MeV).

6. Results

6.1. Required number of sensor layers

The number of layers required to contain the complete proton beam has been found for the different designs studied here. Two additional proton beam energies are included here: 200 MeV and 230 MeV. The necessary dynamic range is defined as the range plus 3 times the range straggling (to accurately measure the tails of the beam): this leads to the required number of layers, listed in Table 2.

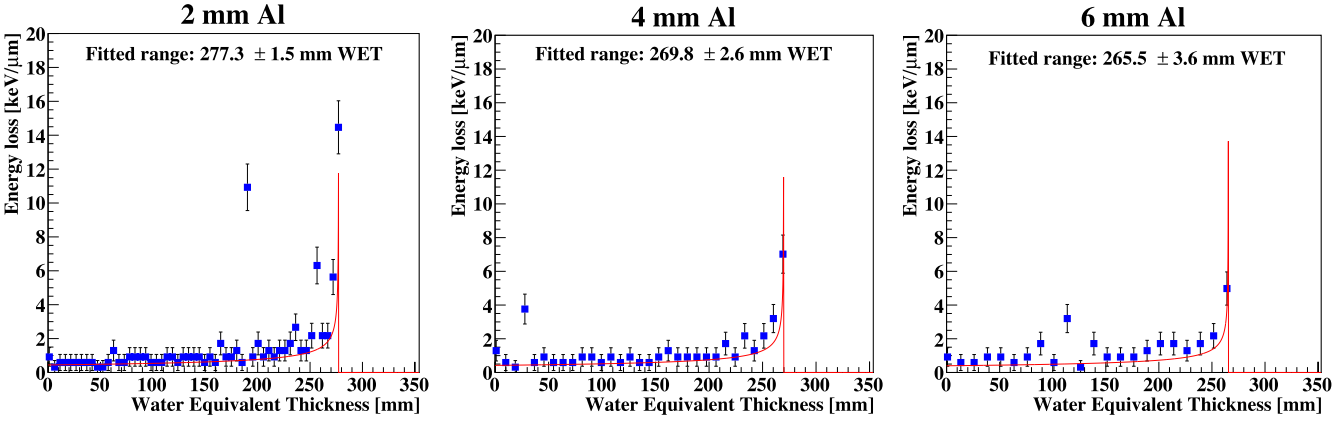

Fig. 3. The deposited energies of individual proton tracks (in three different geometries), overlaid with a Bragg curve fit. The displayed "±" accuracy is the output from the least-squares method applied on an individual proton, and it is not representative for a proton beam of that energy. MC data taken with a 250 MeV beam degraded using a 10 cm water phantom, using the pixel clustering model. Some of the hits have a significantly higher deposited energy—these values can be explained by the Landau distributed energy loss process or by merged clusters.

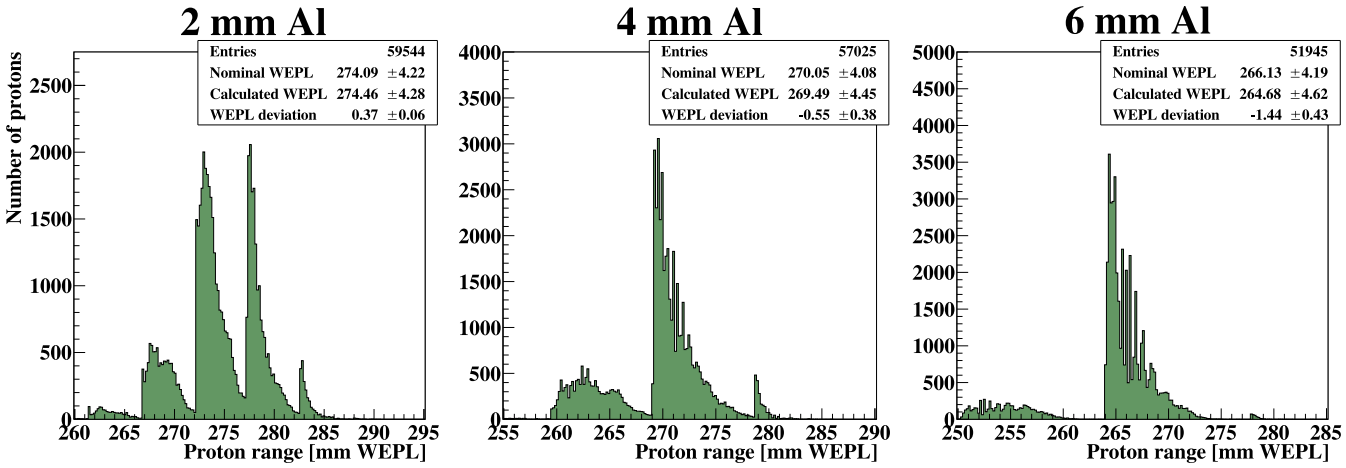

Fig. 4. Distribution of the individual estimated ranges. From this distribution the residual range R and range straggling σ_R of a proton beam is calculated, shown in the text box as "$R \pm \sigma_R$", for the nominal "MC truth" values, for the calculated values and for their difference (as "$\Delta R \pm \Delta\sigma_R$"). The characteristic pattern of the distribution, with regular sudden rises, can be seen in the figure. Each rise in the distribution is in coincidence with the beam reaching a new sensor layer. MC data taken with a 250 MeV monoenergetic proton beam degraded using a 10 cm water phantom [7].

6.2. Efficiency of the track reconstruction

The efficiency of the track reconstruction is shown in Fig. 5 for the different designs under consideration. It has been calculated by repeatedly performing the track reconstruction with n_p concurrent protons, finding the resulting fraction of correctly reconstructed tracks to the total number of tracks (see Section 4.2 for the definition of a correctly reconstructed track).

In the 3 mm design, a 90% efficiency is achieved with a pencil beam intensity of 50.1 protons per readout frame (5.0 million protons per second with 10 µs integration time), and an 80% efficiency is achieved with an intensity of 132.8 protons per readout frame (13.3 million protons per second).

As an example of tracks that are incorrectly reconstructed, 500,000 protons were simulated through a 16 cm phantom in the 3 mm absorber geometry, and reconstructed in batches of $n_p = 100$. After applying the data filters, 286,925 protons tracks remain, of which 11.5% are secondaries (see Section 6.2.1 for more details on the effect of the data cuts). 84.1% of the tracks are correctly reconstructed. The remaining 15.9% are divided into confused tracks (9.4%) which are mainly due to the degrading effects of the pixel clustering model; incompletely reconstructed tracks (5.7%); and tracks both confused and incorrectly reconstructed (0.8%).

6.2.1. Secondary particle discrimination

The efficiency of the different data filters as defined in Section 4.1 were calculated in 500,000 protons simulated through a 16 cm water phantom in the 3 mm absorber geometry. Table 3 shows the fraction of secondaries (including tracks ending in nuclear interactions) after successive application of each of the different data filters. In summary, the reconstructed tracks originally contain 28.0% secondaries, and after filtration this fraction is reduced to 11.6%: the remaining secondaries are similar to the primary tracks in terms of angular distribution, energy deposition in the last layer and range distribution.

6.2.2. Pixel clustering and track reconstruction

In Fig. 6 the central region in a single layer of the detector is shown. Here, the clustering model as described in Section 3.4 has been applied, and the positions of the original hits are reconstructed. During this process, 0–2% of the hits in a layer merge together, and it is not straight-forward to apply data filters to separate them. The merged clusters degrade the quality of the track reconstruction.

If the cluster diffusion effects can be mitigated, we expect that the reconstruction efficiency will increase. A separate analysis was performed where the pixel clustering model was not applied, and the track reconstruction was performed on single-pixel hits. Then, the increase in the proton rate needed to obtain a 90% efficiency can be doubled, from 5.0 million protons per second to 10.2 million protons per second in a pencil beam.

6.3. Accuracy of the range calculation

InFig. 7 the range accuracy is shown throughout the detector's dynamic range for the different designs. The systematic errors are kept within 0.5 mm WET throughout the detector, for the designs having a 5 mm aluminum absorber or less. In the following, a track density of $n_p = 100$ protons per readout is applied, and the pixel clustering effects have been taken into account.

Note that a calibration constant in the order of 0–2 mm has been added to all ranges within a given geometry in the figure. The added numbers are shown in the figure for the respective geometries.

6.3.1. Oscillating error of the range accuracy

There is an oscillation artifact in the range accuracy. It is especially pronounced for the designs with 4 mm and thicker absorbers, and in the 2 mm and 3 mm designs it is negligibly small. The artifact is characterized by a sinusoidal shaped perturbation of the range accuracy. The oscillation has been measured using sinusoidal model fits and Fourier analyses of the range accuracy distributions of Fig. 7. The wavelengths of the oscillations correspond within 1% to the water

Table 2
The number of layers needed to contain a proton beam of 200 MeV and 230 MeV, in the different geometries, when a necessary extra margin corresponding to a distance of three times the range straggling is added [7].

Absorber thickness [mm]	2	2.5	3	3.5	4	4.5	5	5.5	6
Layers needed (250 MeV)	74.9	62.4	53.8	46.8	42.0	37.8	34.5	31.8	29.4
Layers needed (230 MeV)	65.9	54.7	47.0	41.1	36.8	33.1	30.3	27.9	25.8
Layers needed (200 MeV)	52.4	43.7	37.7	32.9	29.5	26.6	24.3	22.5	20.7

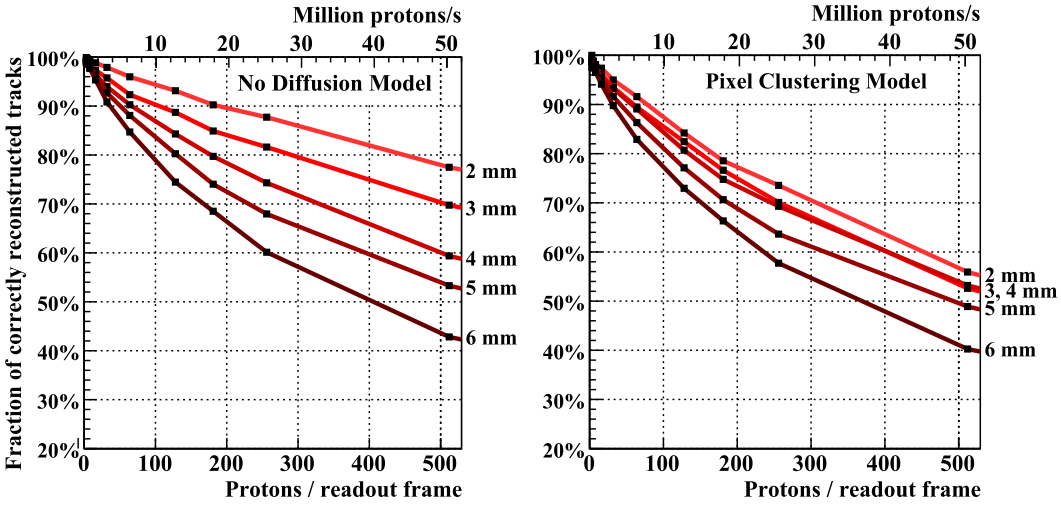

Fig. 5. The fraction of correctly reconstructed tracks, as a function of the particle density, in the different geometries. The definitions of a correctly reconstructed track is given in Section 4.2, and an integration time of 10 µs is assumed. Two scenarios are shown, without (left) and with (right) the application of the pixel clustering model.

Table 3
The efficiency of the different data filters on 500,000 particles propagated through a 16 cm water phantom and into the 3 mm aluminum absorber geometry. The number of tracks after each step is shown, as well as the fraction of secondary tracks: removed during the step, and remaining after the step, respectively (secondaries include tracks ending in nuclear interactions).

	Number of tracks	2nd removed	2nd remaining
Reconstructed tracks	483,287	–	28.0%
After removing high angle tracks	421,810	64.5%	22.7%
After removing short tracks	324,793	53.4%	13.5%
After removing low E_D tracks	281,925	25.7%	11.6%

equivalent spacing between the sensor layers, given by

$$(d_{\text{abs}} + 0.435\ \text{mm})\cdot f_{\text{WET}}, \tag{4}$$

using a WET conversion factor of $f_{\text{WET}} \simeq 2.16$. Here, d_{abs} is the physical thickness of the absorber and $d_{\text{abs}} + 0.435$ mm is the physical spacing between two sensor layers.

The amplitudes of the oscillation are expected to be limited above by $(d_{\text{abs}} + 0.435\ \text{mm})\cdot f_{\text{WET}}/\sqrt{12}$, where the factor $\sqrt{12}$ is the discretization error of a range telescope [22]. In general the amplitudes of the oscillation are well below this limit, and also below 0.5 mm WET if the absorber is thinner than 4.5 mm aluminum, and below 0.2 mm WET for the 3.5 mm aluminum absorber geometry. See Fig. 8 for the relationship between the absorber thickness and the oscillation amplitude.

6.3.2. *Uncertainty of the range calculation*

The uncertainty of the range calculation is calculated as the standard deviation of the fitted range distribution, $\langle\hat{\sigma}_R\rangle$. It is highly dependent on its lower physical limit, which is the statistical range straggling of the proton beam in the detector.

The mean measured range uncertainty $\langle\hat{\sigma}_R\rangle$ varies from 4.4 mm WET measured in the 2 mm aluminum absorber geometry, to 5.2 mm WET measured in the 6 mm aluminum absorber geometry. This is the expected overall uncertainty of the system. However, we need to consider that only a fraction of this number actually is due to the properties of the detection and reconstruction process. The range straggling as found during the MC simulations where interactions in all volumes have been scored (σ_R) varies from 3.9 mm WET in the 2 mm aluminum absorber

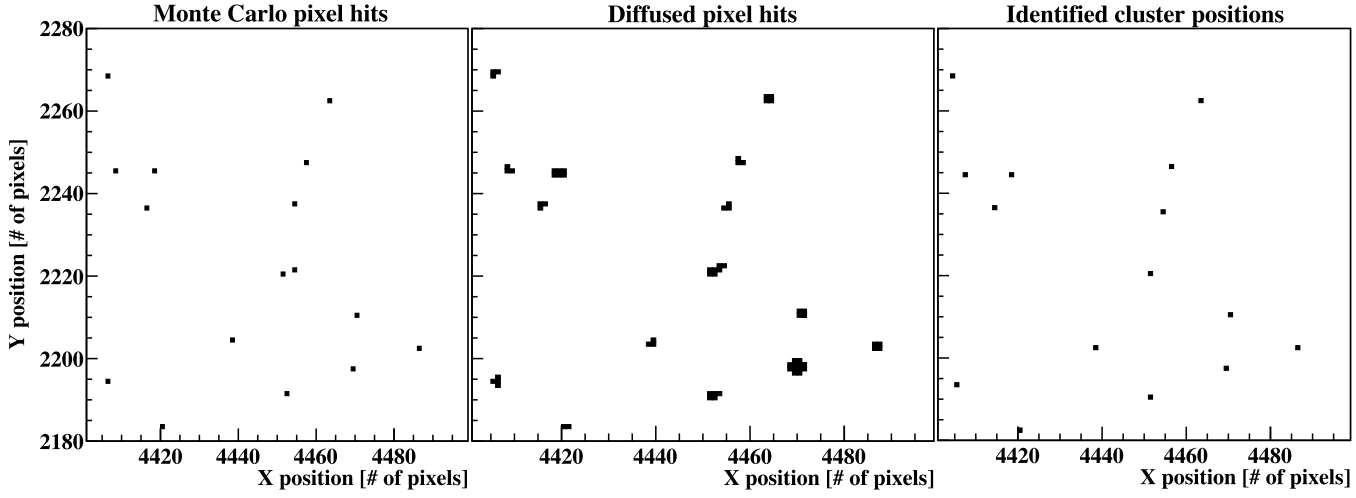

Fig. 6. The pixel clustering model, shown in a central region of 100 × 100 pixels from MC data. **Left:** The single-pixel hits from MC. **Middle:** The pixel diffusion model is applied, where each hit is spread across an area with a shape and size corresponding to its deposited energy. **Right:** The identified cluster positions after analysis. Note the two merged clusters in the center of the image.

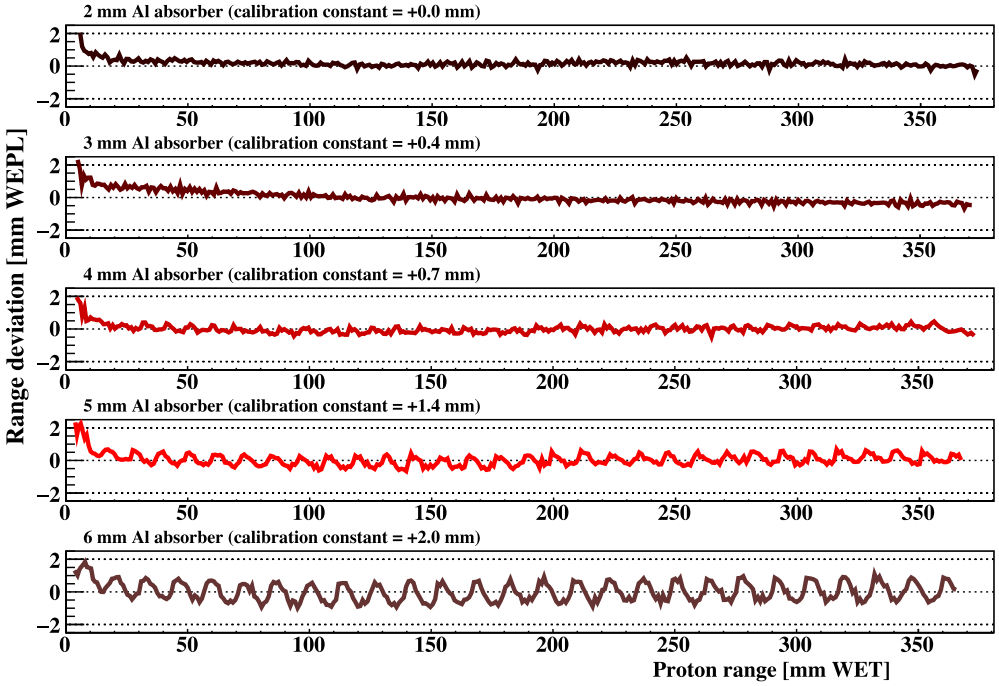

Fig. 7. The range determination accuracy shown as the deviation between the "MC truth" range, and the reconstructed range $\langle \hat{R} \rangle$. For visualization purposes, a calibration constant of 0–2 mm has been added to all ranges within a given geometry in the figure.

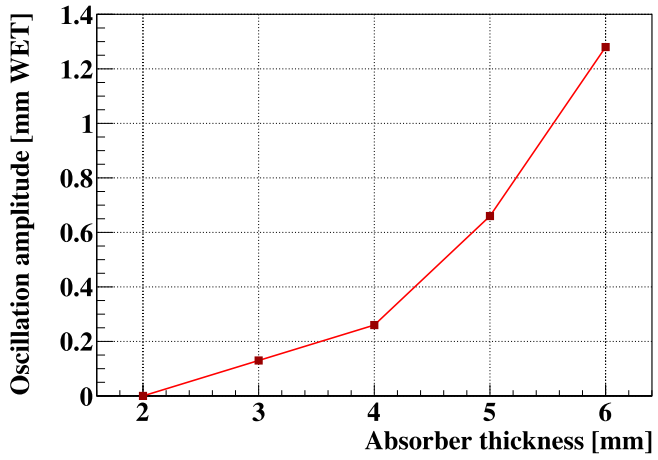

Fig. 8. Measurements of the amplitude of the depth-dependent oscillation of the systematic range uncertainty.

geometry to 3.8 mm WET in the 6 mm aluminum absorber geometry.[2]

Three curves are shown in Fig. 9: the straggling as expected from a 250 MeV beam stopping in pure water; the "MC truth" straggling σ_R calculated from the simulations where the interactions from the full geometry has been scored; and the measured uncertainty $\langle \hat{\sigma}_R \rangle$. The observed fluctuations in the "MC truth" curve can be explained by the longitudinal variations in the range telescope, and by the lower number of primaries used in these simulations. Due to the heterogeneity and denser materials of the detector, we expect the (water equivalent) range straggling in the detector to be above that of water and this is observed.

The added *intrinsic* uncertainty of the reconstruction process and simulation of the detector can be calculated as a quadratic subtraction between the two:

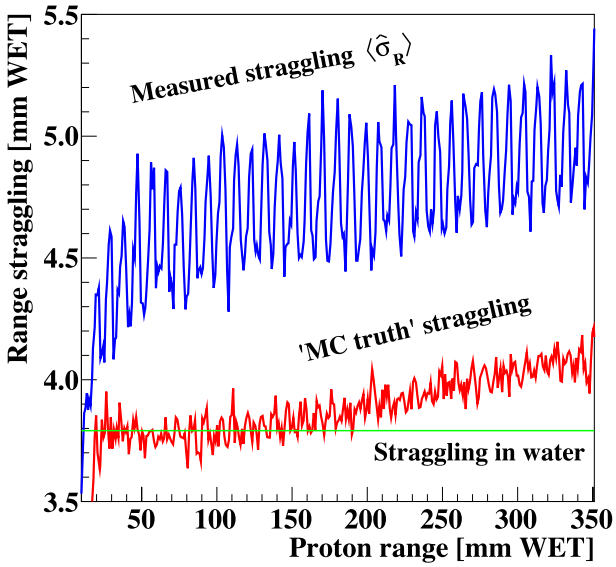

Fig. 9. The measured range straggling $\langle \hat{\sigma}_R \rangle$, together with the actual straggling and the baseline straggling in water, for the 4 mm aluminum absorber geometry.

$$\sigma_{R,\text{Intrinsic}} = \sqrt{\langle \hat{\sigma}_R \rangle^2 - \sigma_R^2} \tag{5}$$

The values for the average intrinsic uncertainty are 2.1 mm WET in the 2 mm aluminum absorber geometry; 2.7 mm WET in the 4 mm aluminum absorber geometry; and 3.5 mm WET in the 6 mm aluminum absorber geometry. These values are shown in Fig. 10 for the different designs.

6.4. Impact on the tracking resolution in the patient due to scattering

One of the required measurements during the proton CT image acquisition is that of the direction of the incoming proton, by using measurements from the first two sensor layers. Any material in the first

[2] The increased fraction of aluminum relative to the copper contents in the PCB reduces the straggling in the thicker absorber geometries.

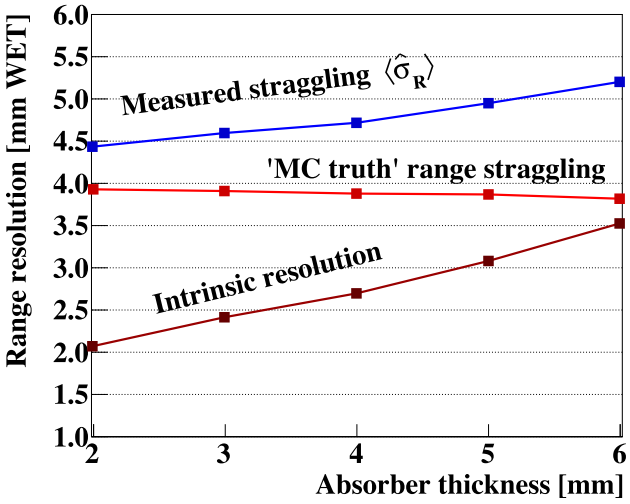

Fig. 10. The range uncertainties of the proposed designs. Shown in the figure is the total uncertainty, the range straggling from the MC truth as well as the added uncertainty which is the quadratic difference between the two. See Table 2 for the number of required layers for the shown designs.

two sensor layers (*i.e.* the sensor chips, the flexible PCB and the carrier backing material) will scatter the incoming protons. The angular dispersion is calculated using the Rossi-Greisen equation of Eq. (1).

Carbon fiber (CF), such as the Mitsubishi DIALED K13D2U [27], has been proposed as a carrier backing material in the low-mass tracker layers due to its thermal properties and mechanical strength. A design applying CF, the flexible PCB board and the ALPIDE chips has been suggested: its material budget is 120 µm aluminum, 160 µm polyimide, 100 µm silicon, 300 µm CF and 30 µm epoxy glue. The resulting radiation length [24] is $X_0 = 14$ cm.

We assume a single scatter event near the first sensor layer, and that the first sensor layer is positioned $L = 10$ cm after the patient as in Bopp et al. [20]. The degraded resolution due to scattering in the first two sensor layers is most precisely calculated by performing a full image reconstruction study, however an approximation is found by projecting σ_{MCS} onto the phantom—given as $L\sigma_{\text{MCS}}$ by Poludniowski et al. [22]. This lateral deflection should be kept as low as possible and below 1 mm.

The resulting value of σ_{MCS} is 7.1 mrad. Hence, the lateral deflection on the object is given by $L\sigma_{\text{MCS}} = 0.7$ mm. To keep this error within 1 mm, we need to apply a distance L of below 14 cm, a task that seems feasible when compared to other systems [5,35].

6.5. Sensitivity analysis of the applied physics models

An additional simulation was performed on the geometry with 3 mm absorbers, with a proton beam degraded by a 16 cm water phantom. In this simulation, the same physics builder list `QGSP_BIC_EMZ` was applied, however the secondary production range cuts and step limitations were reduced to 50 µm. This was done in order to check whether any of the results in this work deviated from the values in the high accuracy simulations.

The former definition of a tagged secondary is used here, *i.e.*, incident secondary particles and also primary particles later undergoing any nuclear interactions. From 500,000 particles generated and tracked in the range telescope, 135,175 secondaries out of 483,287 particles incident on the detector were tagged in the regular simulations (27.97%), while 133,160 secondaries out of 483,552 particles were tagged in the high accuracy simulations (27.54%). The relative difference between the fractions of generated secondaries is 1.54% ± 0.43%, where the uncertainty has been calculated by propagating the respective Poisson uncertainties.

Regarding the effect on the data cuts, it was observed that 12.72% of the incoming tracks had an incoming angle of > 75 mrad in the regular simulations, compared to 12.81% in the high accuracy simulations (relative difference 0.71% ± 0.61%). Furthermore, 8.87% of the tracks had a last-layer energy loss of < 2.5 keV/µm in the regular simulations, compared to 8.83% in the high accuracy simulations (relative difference 0.45% ± 0.71%). In terms of the effect on the range accuracy, $\langle\hat{R}\rangle = 212.28$ mm *WET* in the high accuracy simulations compared to $\langle\hat{R}\rangle = 212.13$ mm *WET* in the regular simulations (relative difference 0.07%).

Except for the secondary production, the relative differences in the compared quantities between the two simulations are < 1%.

7. Discussion

7.1. Design of the range telescope

The design of the pixel-based range telescope should fulfill the following requirements: High accuracy of the range determination; low uncertainty (standard deviation) of the range determination, limited by the inherent proton range straggling; high track reconstruction efficiency, *i.e.* the ability to disentangle and reconstruct a high number of protons in a single readout frame; and other constraints such as economy (number of layers), cooling and mechanical stability.

Based on these requirements and constraints, we find that the detector should be designed with aluminum energy absorption layers between the sensor layers.

In terms of the reconstruction efficiency, a thinner absorber improves the efficiency by a large amount. Hence, the thickness should be as low as possible, and not much above 3 mm.

The range accuracy improvement achieved by using absorbers of thicknesses 3 mm or less is negligible due to the inherent range straggling limit. Thicker absorbers, however, yield a systematic oscillating error in accuracy of the range determination, and at thicknesses of 5 mm and higher this effect will significantly degrade the accuracy.

When considering the overall system complexity, a 4 mm absorber requires fewer sensor layers (37 layers) compared to the 3 mm (corresponding to 47 layers) design, and thus the 3.5 mm could represent an optimal trade-off between efficiency/accuracy and construction constraints. This thickness requires around 41 layers in order to fully contain a 230 MeV proton beam inside the detector (including a 3σ range straggling longitudinal extension).

7.2. Monte Carlo simulations

In this study, several simplifications regarding the detector design have been made. The detector layers have been modeled using slabs of homogeneous materials. Structures in the sensor chips and electronics might introduce systematic errors in the range calculations. In addition, the final material budget of the sensor chips and electronics for a layer might deviate from the design assumed in this study (see Fig. 1). Hence, the results presented in this study are preliminary and should be compared to results from the final experimental system when they are available.

The diffusion of charge carriers have been taken into account by incorporating experimentally measured clusters of appropriate sizes in a pixel clustering model. The pixel clustering model increases the validity of the simulated data, however it also increases the complexity of the reconstruction due to close hits that merge into a single cluster. While tracks are allowed to skip a layer where no expected clusters are found in the position of the extrapolated track, the reconstruction process often continues along the wrong track after a merged cluster. The result is that track reconstructed using this model have a higher fraction of confused track: 9.1%, as compared to 5.9% when the pixel clustering model is not applied; this is in a 16 cm water phantom/3 mm

absorber geometry.

A sensitivity analysis of the applied physics models was performed. The particle transport range threshold was reduced from 0.7 mm to 50 μm, while the maximum step size was reduced from 0.5 mm to 50 μm. The largest deviation was from the secondary production, where a small (< 0.5%) but statistically significant reduction of secondaries was seen in the high-accuracy simulations. No significant changes were observed in the track reconstruction efficiency nor in the range resolution. Furthermore, the short-range secondary production of interest is that happening inside and close to ALPIDE's epitaxial layers. This effect is handled through the pixel clustering model, where the diffusion of the ejected charge carriers is modeled phenomenologically. From this, and in regards to the computational demands of the high accuracy simulations, the simulations were performed using the original parameters.

7.3. Efficiency of the track reconstruction

An incorrectly reconstructed track is expected to have a degrading effect on the reconstructed image. What the degrading effects are, depends on whether the track is incompletely reconstructed or if it is confused with another track. An incompletely reconstructed track is shorter (but within 3σ of the mean range due to the data cut), and will reduce the reconstructed range. Two confused tracks will yield an incorrect initial vector for image reconstruction, and will thus contribute to the noise in the final image: further studies are needed to quantify this effect. In this study, since the scanned object was a homogeneous water phantom, confused tracks did not degrade the range accuracy.

The track reconstruction efficiency increases rapidly with decreasing absorber thickness, and from this perspective, the absorber thickness should be kept below 4 mm and as low as possible. This effect of a thin absorber is reduced somewhat when considering that the degrading effect of merged clusters on the efficiency is proportional to the number of layers (since there is a certain probability of a merging in each layer).

The effects of the clustering might be mitigated through improved algorithms or hardware optimization (such as applying a small reverse-substrate bias voltage). If that is possible, in a pencil beam of 200 protons per readout, when using the 2 mm (4 mm) 6 mm aluminum absorber geometry the fraction of correctly reconstructed tracks is 90% (79%) 68%.

Further optimization of the track reconstruction algorithm and reduction of degrading effects from the pixel clustering will ensure that the reconstruction can be performed at higher beam intensities at high efficiencies.

7.4. Accuracy of the range calculation

Using the proposed geometry, the intrinsic range uncertainty is expected to be 2.6 mm WET, compared to the range straggling of 3.8 mm WET that is added to this number in quadrature.

The dynamic range of the range telescope, given by the region with uniform range uncertainty and uniform range accuracy, is between 10 mm WET and 360 mm WET in the detector, or in terms of proton energy, between 35 MeV and 245 MeV. The reduced accuracy in the first 10–20 mm is expected due to the low residual range of the protons, only traversing a few detector layers. A slight large-scale systematic variation is also seen (as in the 3 mm absorber geometry). This effect is not fully understood, but is expected to be due to a non-constant track reconstruction efficiency or due to energy/range/water equivalent range conversions.

A systematic oscillating error is introduced to the range determination accuracy due to the layer structure of the detector. The origin of the artifact is that the range straggling distribution of a proton beam spans several sensor layers (see Fig. 4). The range accuracy depends on the number of sensor layers covered, and on the position of the mean value of the range distribution relative to the position of the adjacent sensor layers. The more sensor layers that are covered by the range straggling distribution (*e.g.* thinner energy absorbers), the smaller the oscillation artifact. This was also seen in the proof-of-concept prototype detector [6], where range distributions that covered two sensor layers had a significantly higher range accuracy compared to range distributions that only covered a single sensor layer.

By applying 3.5 mm thin aluminum absorbers, the oscillation is kept below 0.2 mm WET. This is a systematic uncertainty, hence it is not possible to reduce it by increasing the number of protons per projection.

7.5. Impact of the tracking resolution in the patient due to scattering

The first tracker layers are used to calculate the incoming proton trajectory. To keep these first layers low-mass, a thin layer of carbon fiber for stabilization is proposed. The planned total mass of the low-mass layers is 0.5% X_0, ensuring that the scattering angle of a proton in the energy range of interest is ~7 mrad (from the Rossi-Greisen equation). Poludniowski et al. [22] propose a limit of 1 mm on the uncertainty of this scattering angle projected onto the imaged object: this corresponds here to keeping the distance between the imaged object and the tracker layers to <14 cm. This distance is also expected to have an effect on the performance of the track reconstruction—the more spread out the pencil beam is (increased distance), the easier it is to correctly reconstruct the tracks (less particle density).

8. Conclusion

In this study we have investigated the performance of different conceptual designs of a pixel-based range telescope using MC simulations together with the analysis framework developed for a proof-of-concept prototype investigated earlier [6]. Specifically, the analysis was performed by combining tracking of individual protons and Bragg curve modeling of each proton's energy loss. The goal was to find the accuracy of the range calculations and evaluate the track reconstruction algorithms in designs applying energy degrading absorbers of 2–6 mm aluminum.

A charge clustering model has been implemented using data from a 2018 experimental beam test at Heidelberg Ion Therapy facility acquired using the ALPIDE pixel sensor chips to be applied in the range telescope. This model increases the validity of the simulations, and we observe a reduction of the tracking efficiency due to this effect.

The proposed first low-mass tracker layers are expected to introduce a positional uncertainty on the proton's position at the object exit in the order of 0.7 mm, below the limit of 1 mm from Poludniowski et al. [22].

The detector is expected to have the capability of tracking 5–20 million protons per second, assuming realistic electronics- and design proposals. The range uncertainties are close to the range straggling limit, and any systematic errors in the range determination are kept below 0.3 mm WET throughout the detector. By considering the presented results, the optimal material choice for the energy-absorbing layers is 3.5 mm aluminum.

Acknowledgements

An earlier version of this text is included in the first author's PhD dissertation [7], a project which was supported by Helse Vest (Western Norway Regional Health Authority, Stavanger, Norway) grant [911933].

References

[1] Johnson RP. Review of medical radiography and tomography with proton beams. Rep Prog Phys 2018;81(1):016701https://doi.org/10.1088/1361-6633/aa8b1d.
[2] Paganetti H. Range uncertainties in proton therapy and the role of Monte Carlo simulations. Phys Med Biol 2012;57(11):R99–117. https://doi.org/10.1088/0031-

9155/57/11/R99.
[3] Schulte RW, Penfold SN, Tafas JT, Schubert KE. A maximum likelihood proton path formalism for application in proton computed tomography. Med Phys 2008;35(11). https://doi.org/10.1118/1.2986139. 4849.
[4] Collins-Fekete CA, Volz L, Portillo SKN, Beaulieu L, Seco J. A theoretical framework to predict the most likely ion path in particle imaging. Phys Med Biol 2017;62(5):1777–90. https://doi.org/10.1088/1361-6560/aa58ce.
[5] Esposito M, Waltham C, Taylor JT, Manger S, Phoenix B, Price T, et al. PRaVDA: the first solid-state system for proton computed tomography. Phys Med 2018;55:149–54. https://doi.org/10.1016/j.ejmp.2018.10.020.
[6] Pettersen HES, Alme J, Biegun A, van den Brink A, Chaar M, Fehlker D, et al. Proton tracking in a high-granularity digital tracking calorimeter for proton CT purposes. Nucl Instrum Methods Phys Res A 2017;860:51–61. https://doi.org/10.1016/j.nima.2017.02.007.
[7] Pettersen HES. Digital tracking calorimeter for proton computed tomography [Ph.D thesis]. Norway: University of Bergen; 2018.
[8] Jan S, Santin G, Strul D, Staelens S, Assie K, Autret D, et al. GATE: a simulation toolkit for PET and SPECT. Phys Med Biol 2004;49(19):4543. https://doi.org/10.1088/0031-9155/49/19/007.
[9] Jan S, Benoit D, Becheva E, Carlier T, Cassol F, Descourt P, et al. GATE V6: a major enhancement of the GATE simulation platform enabling modelling of CT and radiotherapy. Phys Med Biol 2011;56(4):881–901. https://doi.org/10.1088/0031-9155/56/4/001.
[10] Sarrut D, Bardiés M, Boussion N, Freud N, Jan S, Létang JM, et al. A review of the use and potential of the GATE Monte Carlo simulation code for radiation therapy and dosimetry applications. Med Phys 2014;41(6):064301https://doi.org/10.1118/1.4871617.
[11] Agostinelli S, Allison J, Amako K, Apostolakis J, et al. Geant4-a simulation toolkit. Nucl Instrum Methods Phys Res A 2003;506(3):250–303. https://doi.org/10.1016/S0168-9002(03)01368-8.
[12] Allison J, Amako K, Apostolakis J, Arce P, Asai M, Aso T, et al. Recent developments in Geant4. Nucl Instrum Methods Phys Res A 2016;835:186–225. https://doi.org/10.1016/j.nima.2016.06.125.
[13] Aglieri Rinella G. The ALPIDE pixel sensor chip for the upgrade of the ALICE inner tracking system. Nucl Instrum Methods Phys Res A 2016;845:583–7. https://doi.org/10.1016/j.nima.2016.05.016.
[14] Abelev B, Adam J, Adamová D, Aggarwal MM, Aglieri Rinella G, Agnello M, et al. Technical design report for the upgrade of the ALICE inner tracking system. J Phys G 2014;41(8):087002https://doi.org/10.1088/0954-3899/41/8/087002.
[15] Grøttvik OS. Design of high-speed digital readout system for use in proton computed tomography (MSc thesis). Norway: University of Bergen; 2017.
[16] Llopart X, Ballabriga R, Campbell M, Tlustos L, Wong W. Timepix, a 65k programmable pixel readout chip for arrival time, energy and/or photon counting measurements. Nucl Instrum Methods Phys Res A 2007;581(1):485–94. https://doi.org/10.1016/j.nima.2007.08.079.
[17] Gehrke T, Burigo L, Arico G, Berke S, Jakubek J, Turecek D, et al. Energy deposition measurements of single1H,4He and12C ions of therapeutic energies in a silicon pixel detector. J Instrum 2017;12(04):P04025. https://doi.org/10.1088/1748-0221/12/04/P04025.
[18] Maczewski L. Measurements and simulations of MAPS (Monolithic Active Pixel Sensors) response to charged particles – a study towards a vertex detector at the ILC [PhD]. University of Warsaw; 2010. ArXiv:1005.3710.
[19] Nooren G, Haas AP, Peitzmann T, Reicher M, Rocco E, Röhrich D, et al. The FoCal prototype – an extremely fine-grained electromagnetic calorimeter using CMOS pixel sensors. J Instrum 2018;13(01):P01014. https://doi.org/10.1088/1748-0221/13/01/P01014.
[20] Bopp C, Rescigno R, Rousseau M, Brasse D. The impact of tracking system properties on the most likely path estimation in proton CT. Phys Med Biol 2014;59(23):N197–210. https://doi.org/10.1088/0031-9155/59/23/N197.
[21] Rossi B, Greisen K. Cosmic-ray theory. Rev Mod Phys 1941;13:240–309. https://doi.org/10.1103/RevModPhys. 13.240.
[22] Poludniowski G, Allinson NM, Evans PM. Proton radiography and tomography with application to proton therapy. Br J Radiol 2015;88(1053):20150134. https://doi.org/10.1259/bjr.20150134.
[23] Gómez Marzoa M. Innovative low-mass cooling systems for the ALICE ITS Upgrade detector at CERN [PhD]. Lausanne, CH: École Polytechnique Fédérale de Lausanne; 2016.
[24] Particle Data Group. Atomic and Nuclear Properties of Materials for more than 300 materials; 2015.http://pdg.lbl.gov/2015/AtomicNuclearProperties/ [accessed 12.01.2018].
[25] Touloukian YS, Powell RW, Ho CY, Klemens PG. Thermophysical properties of matter – the TPRC data series. Thermal Conductivity – Nonmetallic Solids, vol. 2. Defense Technical Information Center; 1971.
[26] Goodfellow Inc. Polymethylmethacrylate material information; 2018. http://www.goodfellow.com/E/Polymethylmethacrylate.html [accessed 01.10.2018].
[27] Mitsubishi Chemical. K13D2U datasheet; 2018.https://www.900gpa.com/en/product/fiber/CF_00D7088B15 [accessed 28.12.2018].
[28] Rescigno R, Bopp C, Rousseau M, Brasse D. A pencil beam approach to proton computed tomography. Med Phys 2015;42(11):6610–24. https://doi.org/10.1118/1.4933422.
[29] Berger MJ, Coursey JS, Zucker MA, Chang J. ESTAR, PSTAR, and ASTAR: computer programs for calculating stopping-power and range tables for electrons, protons, and helium Ions. Gaithersburg, MD: National Institute of Standards and Technology; 2005.
[30] Grevillot L, Frisson T, Zahra N, Bertrand D, Stichelbaut F, Freud N, et al. Optimization of GEANT4 settings for Proton Pencil Beam Scanning simulations using GATE. Nucl Instrum Methods Phys Res B 2010;268(20):3295–305. https://doi.org/10.1016/j.nimb.2010.07.011.
[31] Pettersen HES, Chaar M, Meric I, Odland OH, Sølie JR, Röhrich D. Accuracy of parameterized proton range models; a comparison. Radiat Phys Chem 2018;144C:295–7. https://doi.org/10.1016/j.radphyschem.2017.08.028.
[32] Mager M. ALPIDE, the Monolithic Active Pixel Sensor for the ALICE ITS upgrade. Nucl Instrum Methods Phys Res A 2016;824:434–8. https://doi.org/10.1016/j.nima.2015.09.057.
[33] Pettersen HES, Meric I, Odland OH, Shafiee H, Sølie JR, Röhrich D. Proton tracking algorithm in a pixel based range telescope for proton computed tomography. EPJ WEB CONF. in Press.
[34] Bortfeld T. An analytical approximation of the Bragg curve for therapeutic proton beams. Med Phys 1997;24(12):2024–33. https://doi.org/10.1118/1.598116.
[35] Johnson RP, Bashkirov V, DeWitt L, Giacometti V, Hurley RF, Piersimoni P, et al. A fast experimental scanner for proton CT: technical performance and first experience with phantom scans. IEEE Trans Nucl Sci 2016;63(1):52–60. https://doi.org/10.1109/TNS.2015.2491918.